CALORIMETRY

V.E. Viola and R. Bougault

In any attempt to describe a system in terms of thermodynamic variables, a knowledge of heat content is fundamental. For hot nuclei, this energetic factor is usually expressed in terms of excitation energy per nucleon, E*/A. Because nuclei are finite systems, size is important. Thus, it is necessary to determine both the heat content E* and the number of nucleons A that characterize the disintegrating ensemble. In this chapter we examine the methods by which E* and A are evaluated, as well as associated errors.

Ideally, the calorimetric measurement of E*/A requires an apparatus that collects the total energy (K), charge (Z) and mass (A) of all charged particles and neutrals that compose a given event. With this information the event can be re-constructed, permitting calculation of E* and A of the source, where

$$E^*_{source} = \sum_i K_{cp}(i) + \sum_j K_n(j) - Q(i,j) \qquad (1)$$

and

$$Z_{source} = \sum_i Z_{cp}(i); A_{source} = \sum_i A_{cp}(i) + \sum_j A_{cp}(j) \qquad (2)$$

Here K_{CP} is the kinetic energy for all LCPs (H and He), IMFs (3=Z? 20) and heavy residues (A? 20). K_n is the kinetic energy for neutrals (neutrons and gammas), and the removal energy (- Q) is the negative of the reaction Q-value.

However, no calorimeter is perfect. Thus in order to extract E*/A from data, one must construct a filter that considers numerous sources of energy and mass loss. Among these are:

(1) Acceptance limitations imposed by the construction of the apparatus and the properties of its constituent detectors;

(2) Physics uncertainties, most importantly the criteria for accepting only particles that classify as "equilibrium-like"; i.e., preequilibrium and mid-rapidity emissions must be removed from the sums for Eqs. (1) and (2).

(3) Finally, since no two detector arrays have the same acceptance, differences in protocols for converting the filtered data into E*/A must be examined.

In the following sections, these issues are surveyed along with their inherent uncertainties. The analysis is drawn from those references in Table I, which are representative (but not complete) examples of the procedures currently employed in nuclear calorimetry.

E* REFERENCES		
pbar + A	**Berlin n/cp Ball:**	PLB **423**, 21 (1998);
p, p,3He + A	**ISiS:**	PRL **77**, 1230 (1996); PRC **64**, 064603&4 (2001)
p, 4He, C + A	**FASA:**	NPA **700**,457 (2002); NPA **709**, 392 (2002)
A + C	**EOS:**	PRC **62**, 024616 (2000)
A + A	**ALADIN:**	PRL **75**, 1040 (1995); NPA **607**, 457 (1996)
"	**INDRA:**	NPA **686**, 537 (2001); NPA **700**, 555 (2002)
"	**TAMU:**	PRC **55**, 227 (1997); PRC **62**, 034607 (2000)
"	**CHIMERA:**	E. Gallichet, commun.
"	**LAVAL ARRAY**	PRL **77**, 462 (1996)
"	**SUPERBALL:**	PRC **64**, 034603 (2001)

The Detector Filter

The existing multifragmentation detector arrays are of various types. Most charged-particle detection involves some combination of silicon, gas-ionization chamber and CsI scintillator telescopes for Z (and in some cases A) identification. The EOS experiment employed a time-projection chamber (TPC) and ALADIN utilized a magnetic spectrometer. Neutrons have been measured with large tanks of Gd-loaded scintillator liquid an via time-of-flight techniques.

In developing a reliable detector filter, several factors must be considered, as enumerated below. The filter must then be tested in insure that it reproduces input from a theoretical model.

- Solid-angle acceptance – In constructing any detector array, allowance must be made for beam entry/exit ports and any shadowing by the target. Because of kinematic focusing, these problems become less severe as the mass and energy of the projectile increase. For light-ion reactions, for which the laboratory angular distributions are nearly isotropic, target shadowing must be treated carefully. The resulting geometric-acceptance factor must then be applied to all events, which due to fluctuations may either over- or under-correct the data. For most detectors geometric acceptance ranges from about 75% to the nearly complete acceptance for the EOS TPC.
- Detector granularity – since the final states in multifragmentation reactions may involve large numbers of particles, high detector granularity ($N > 100$) is essential to minimize multiple-hit misidentification of fragments. In addition, angular information is required to test whether events classified as "equilibrium-like" meet the isotropic emission standard for a randomized system.

· Detector Characteristics – Charged Particles

– Thresholds: The low-energy component of spectra measured with ΔE-E particle identification telescopes is constrained by the thickness of the ΔE element. Lowest thresholds are obtained with gas-ionization chambers essential for light-ion-induced reactions. The kinematic boost for fragments produced in heavy-ion reactions permits the use of higher stopping power, Si and CsI ΔE elements. Ideally, corrections to the energy sum must be made for the missing part of the spectrum due to threshold effects.

– Detector Resolution: Si semiconductor detectors provide the highest energy resolution for determination of energy-loss and total energy K. For this reason Si-Si telescopes can provide both Z and A information for a significant range of the multifragmentation spectrum, limited by the minimum ΔE thickness and maximum E thickness. Because of their minimum stopping power, gas ionization chambers are most effective as ΔE detectors for fragments with low kinetic energy per nucleon. Although CsI provides the poorest energy resolution, the ability to form very thick crystals makes it ideal for detecting the most energetic particles. Depending on the energy of the emitted particles, TPC and spectrometer measurements usually yield energy resolution intermediate between Si and CsI for IMFs and heavier fragments.

· Detector Characteristics – Neutrons

The greatest experimental uncertainty in determining the total kinetic energy sum is the contribution from neutron emission, for which multiplicities are comparable to or greater than charged particles. The energy associated with gamma-rays is usually assumed to be small. The neutron kinetic energy spectrum is measured via time-of-flight techniques, using fast

plastic/liquid scintillators. Such measurements sample only a small fraction of 4π because of the spatial limitations imposed by flight path. Hence, they yield only limited multiplicity information. Neutron multiplicities and charged-particle correlations have been determined with $\sim 4\pi$ tanks of Gd-loaded liquid scintillator. Neutron detection must be corrected for energy-dependent efficiency losses, which contributes the multiplicity uncertainty. Few experiments have been performed with simultaneous Z and A identification for the entire multifragmentation yield. The EOS TPC provides the broadest spectrum of Z and A identification and the momentum acceptance of the ALADIN spectrometer permits A detection over a significant mass range. Heavy fragment masses employed by most other arrays rely on mass balance techniques and/or charge information, with N/Z assumptions.

· Statistics

The total number of events for highly-excited nuclei (E*/A ? 2 MeV) is a function of both the maximum event rate of the detector array and the availability of accelerator time. TPC and neutron-tank measurements are limited in counting rate, so statistics are usually low. Detector-array studies of A + A reactions exhibit a wide range of statistics, depending on the number of systems studied in a finite amount of accelerator time. Most of the light-ion data have accumulated large numbers of events by using secondary beams over long (months) running time.

Physics Issues

In addition to mechanical and detector response contributions to the filter, several physics issues must be addressed, the most important of which is the selection of "equilibrium-like" events. The time evolution of nuclear reactions above the Fermi energy extends from the initial collision phase to an eventually randomized state that decays statistically. Particle

emission occurs at all stages as radial projectile energy is converted into internal excitation energy. Selection of only those emissions that have a statistical origin is therefore a nontrivial problem. Other physics issues also come into play; e.g. neutron-proton correlations, kinematic effects on the event reconstruction process in A + A reactions, and the primary N/Z ratio of the emitted fragments. Below, these contributions to the filter are discussed.

· Preequilibrium and Mid-rapidity Emission

Two essential first-order tests of a randomized system are the Maxwellian nature of its spectra and the forward-backward symmetry of its particles.

In Figs. 1-3 spectra are shown for GeV-light-ion-induced reactions. These spectra best illustrate the prompt statistical emission ambiguity, since there is only a single emitting source and difference between the laboratory and center-of-mass velocities is small (~ 0.01 c). The left frame of Fig. 1 shows neutron spectra at a far backward angle for the 1.2 GeV $\bar{p}$ reaction on several targets. Two components are present: a low-energy Maxwellian peak and an exponential high-energy tail. The former is associated with "equilibrium-like" behavior and the latter with preequilibrium emission. Separating these two components on an event-by-event basis is not a transparent procedure.

The right-hand frame of Fig. 1 shows inclusive spectra for LCPs and IMFs measured in the 8 GeV/c $\pi^- + {}^{197}$Au reaction. These spectra have been decomposed using a two-component moving-source model that assumes a statistical model for the low-energy component (dashed line) and an arbitrary Maxwellian function for the high-energy tail (dotted line). Preequilibrium emission is seen to be primarily important for LCPs and decreases in significance as the fragment charge increases.

In the left-hand frame of Fig. 2 the angular dependence of the spectra is shown, along with the moving-source decomposition. Preequilibrium emission is forward-focused, whereas the statistical component (when integrated) is nearly isotropic in the lab system. By demanding forward-backward isotropy of the statistical component, the average source velocity can be determined, as well as the fragment energy at which the preequilibrium contribution is negligible (cutoff energy). The average source velocity and cutoff energy can be determined from moving-source fits to the data. These are then incorporated into the filter, using a Z-dependent function for the cutoff energy. As examples of how the separation between statistical and preequilibrium affects the determination of E*/A, Fig. 3 compares the excitation-energy distribution for the π^- + ^{197}Au reaction using both the EOS cutoff energy of $K_{CP}/A = 30$ MeV and that employed by ISiS, K = 30 MeV for protons and $K_{CP} = 9Z + 30$ MeV for higher fragment charges. The EOS prescription enhances the probability for high E*/A values, leading to the difference of nearly 200 MeV at the 1% probability level. (In all other regards the 1 GeV ^{197}Au + ^{12}C results from EOS are consistent with the 8GeV/c π^- + ^{197}Au results from ISiS).

The preequilibrium/statistical separation process is further complicated by the evolution of the spectra with E*/A as shown in the right-hand panel of Fig. 2. Here H and He spectra, which dominate the preequilibrium yield, are shown for E*/A = 2-4, 4-6 and 6-9 MeV bins. The ISiS cutoff assumptions are heavily based on the lower energy bin. However, as E*/A increases, the spectra evolve into a single Maxwellian distribution, so that separation of the two components becomes more ambiguous. For A + A reactions the situation is complicated by the existence of three sources: projectile-like, target-like and mid-rapidity, each of which is then subjected to the same constraints as for light ions. The behavior of the three sources is illustrated in Fig. 4, which shows invariant cross section distributions for Z = 3 , 6 and 9 fragments as a

function of bombarding energy for peripheral $^{197}Au + ^{197}Au$ data from the INDRA/GSI collaboration. The separation of the Coulomb rings for the projectile-like source (high y) from the target-like source (low y) becomes increasingly distinct as the bombarding energy increases. For Z = 3 the preequilibrium skewing of the spectra along the beam axis (x = 0) is apparent. For Z = 6 and 9 this contribution becomes less important. At lower bombarding energies, the mid-rapidity source masks the projectile-like and target-like statistical spectra, complicating their separation, a procedure that entails the same type of arbitrary assumptions that exist for the light-ion data. By applying such cuts for more central collisions, a single statistical source can be identified that is isotropic in the source frame.

The effect of assumptions about nonequilibrium emission is presented in Fig. 5 for peripheral $^{197}Au + ^{197}Au$ reaction energies of 600, 800 and 1000 GeV, data obtained by the ALADIN group. In the caloric curve shown in the upper left panel, the E*/A distribution extends up to 25 MeV for the 1000A MeV data, and the two caloric curves are not consistent. In the central panel, the relative contributions of neutrons, LCPs and IMF indicates that the nonequilibrium contributions to the spectra grow significantly between 600 A and 100 A MeV. As shown in the lower-right panel, when corrections are made to eliminate nonequilibrium components, the caloric curves overlap, with maximum E*/A values reduced to E*/A $\approx$ 12 MeV for both bombarding energies.

Neutrons

Evaluation of E*/A via Eqs. (1) and (2) requires a knowledge of the kinetic energy and multiplicity of the neutrons in an event. Because of the inherent difficulties in measuring neutrons, as discussed previously, only a few measurements exist that measure neutrons and charged particles simultaneously. Important examples are the studies carried out with the Berlin Ball, the Rochester Superball and the Texas A&M NIMROD systems. For those arrays that detect only charged particles, the existing measurements of neutron-proton multiplicity correlations and spectra must be relied upon to estimate the missing neutron contribution to E*/A.

Neutron spectra are shown in Fig. 1. In Fig. 6 the neutron-light-charged particle multiplicity correlations are compared for A + A and light-ion reactions. Two systems are shown: 28 MeV/A Xe + Bi and 1.2 GeV $\bar{p}$ + several targets. Both cases behave similarly, with a target mass-dependence that favors an increasing growth in the n/LCP ratio with increasing target mass. The total particle multiplicity is known to be strongly correlated with excitation energy. For heavy targets the neutron multiplicity increases rapidly with excitation energy up to E*/A ~ 2 MeV, while charged-particle emission remains low due to Coulomb inhibition. At higher excitation energies, the probability for additional neutron emission is approximately balanced by LCP emission.

The top panel of Fig. 6 compares the Xe + Bi multiplicity correlation with the average predicted by two multifragmentation models, SMM and MMMC with an input excitation energy of 0.9 GeV. Both models give similar results [check this], although falling below the data centroid. By increasing E* to 1.0 GeV, the predicted n/LCP ratio gives reasonable agreement

with the data. The effect of increased bombarding energy on the n/LCP correlation is indicated for the Xe + Bi case in Fig. 7. No strong dependence is observed.

For heavy targets the relative insensitivity of the n/LCP ratio to colliding system or bombarding energy, as well as the general agreement with models, provides guidance in accounting for the missing neutron fraction of E*/A in arrays that measure only charged particles. Various approaches have been followed: use of model calculations calibrated to the LCP multiplicity, or direct use of the experimental multiplicity correlation centroids. An alternative is to employ a mass-balance approach, as determined from the experimental event structure. Fig. 8 illustrates the effectiveness of such techniques, using the 1.2 GeV $\bar{p}$ + ^{197}Au results. SMM (dotted curve) and SIMON-evaporation (dashed line) provide a reasonable description of the data for M_{LCP} ? 3 (E*/A ~ 2 MeV). Mass conservation (open squares) is not satisfactory in this case, although in some instances the nature of the data may provide a more satisfactory fit.

The primary difficulty in determination of the neutron contribution to E* and the source mass A_{source} is that the neutron tanks provide multiplicity information (good for A_{source}) but not neutron energies, while the time-of-flight method provides energies (good for E_n but only limited multiplicity data. By use of LCP-calibrated models, it is possible to obtain a reasonable approximation to the total excitation energy contributed by neutrons. However, in doing so, one is employing averages that fail to introduce fluctuations in M_n and K_n.

Additional Factors

While nonequilibrium and neutron emissions constitute the major sources of uncertainty in the determination of E*/A, several other factors must be taken into account, as discussed in the following.

- Source Reconstruction

Among the various multifragmentation programs, calculation of the properties of the emitting source – charge, mass and velocity – are usually detector-array-dependent. For light-ion + A reactions, for which there is only one source, reconstruction depends on the acceptance of the array. The EOS TPC measurements provide nearly complete charged-particle detection, as shown in the left-hand from of Fig. 9, from which the statistical component of an event can be extracted. For A+A reactions one must perform an invariant cross section analysis, following the schematic decomposition picture shown in the center frame of Fig. 9, in order to isolate projectile- and target-like sources, as well as any possible fusion-like remnant. Fig. 4 illustrates the results of such an analysis. Total charge results for projectile-like fragments from ^{197}Au + ^{197}Au studies of the MULTICS/MINIBALL are presented in the right-hand frame of Fig. 9. In nearly all cases, the emitting source mass is determined from the A/Z ratio of the heavy collision partner(s). Velocities for the statistical source can be determined from the forward-backward symmetry requirement for the invariant cross-sections.

Representative protocols for evaluating the source properties are described in the next section.

- Fragment N/Z Ratio

To achieve optimum reconstruction of a multifragmentation event, it is necessary to know the mass of the primary fragments. This information is relevant to determining the source

mass and the Q-value calculation. Several procedures have been employed to convert the observed secondary yields into primary yields. In cases where both Z and A are measured, models can be used to obtain the primary fragment mass. However an important consideration is whether the fragments are emitted hot or cold. In most cases, only the fragment charge is measured for all but the lightest elements. Various approaches have addressed the conversion of the data to primary yields. One is to use the N/Z ratio of the cold fragments, the composite system, or some combination of the two. Another is to use the N/Z ratio of IMFs emitted in reactions of protons with heavy nuclei at energies below 500 MeV, where secondary emission should be small.

- Expansion Energy

Finally, any internal energy used to expand the hot source, must be subtracted from the excitation energy sum of Eq. (1). As shown in Fig. 10, for light-ion reactions this is a small, but non-negligible contribution at high excitation energies. For A + A reactions, compression effects produce considerable expansion and therefore can contribute a significant amount to the E* sum at high excitation energies. This correction also accounts for the bombarding-energy dependence of E* shown in Fig. 5.

E*/A Protocols

The procedures for converting raw experimental data to E*/A differ for every multifragmentation. Once detector calibration and filter development is complete, the salient variables can be applied to Eqs. (1) and (2). In this section, several methods are described that are representative of the approaches that have been employed.

- Model-Based Calorimetry

In the $\bar{p}$ studies of the Berlin Neutron/Silicon Ball, E* is determined by comparison of the light-charged particle multiplicity with that predicted by the evaporation code GEMINI at a given excitation energy. Since IMF multiplicities are rarely greater than one in this experiment, the use of an evaporation code is appropriate. For the higher-energy LCP + A studies employed by the FASA group, an empirical parameter α is obtained from comparison of observed charged-particle multiplicities with the multiplicity distribution predicted by a hybrid RC + SMM model. The excitation energy is then taken to be a function α times the predicted excitation energy Below, we summarize the calorimetry procedures used in several of the systems that calculate E*/A on an event-by-event basis.

- Calorimetry in Highly Asymmetric Systems

EOS: $Z_{src} = Z_{tgt} - \sum_i Z_i^{neq}$

$A_{src} = A_{tgt} - [\ \sum_i Z_i^{neq} + 1.70\ M_p^{neg}\ ]$

$M_n = A_{src} - \sum_i A_i^{thermal}$

$\langle E_n \rangle = M_n \cdot (3/2)T$; $a = (A/13)\ MeV^{-1}$

ISiS:

$Z_{src} = Z_{tgt} - \sum_i Z_i^{neq}$

$A_{src} = A_{tgt} - [\sum_i Z_i^{neq} + 1.93\ M^{neg}_p]$

A_{IMF} : Korteling, with the assumption that no charged-particle decay of IMFs has occurred.

ALADIN:

$$(Z, A)_{src} = \sum_{i} [(Z,A)_{proj} - (Z, A)_{fireball}] ; y > 0.7 y_{beam}$$

M_n: Measured-thermal

- E_n: Measured

M_H: p:d:t from literature

$M_{Z=1}$, A_{src} from $1.3 < (N/Z)_{souce} < 1.5$

A_{IMF}: EPAX ($Z > 3$)

$A_{He, Li}$, randomly according to measured mass distributions for Z = 2, 3

Conclusions

From analysis of the filtered multifragmentation data, all three terms in Eq. (1) – charged particle kinetic energies, neutron kinetic energies and removal energy (–Q) – are found to have significant weights in the excitation-energy sum. In the upper panel of Fig. 11 to relative kinetic energy percentages are shown for LCPs, neutrons and IMFs as a function of E*/A. Neutrons and LCPs are roughly equivalent, accounting for 20-30% over the entire E*/A range. IMFs do not become signicicant until about E*/A ~ 3-4 MeV, reaching a maximum of 12-14% near E*/A ~ 6 MeV. Above E*/A ~ 6 MeV, all three percentages remain nearly constant. As is apparent from the previous discussions, these percentages vary, depending on assumptions about nonequilibrium emission, neutrons, etc.

The bottom frame of Fig. 11 compares to the percentage of the E* sum for total kinetic energy release with that for the removal-energy derived from event reconstruction. For low excitation energies, the kinetic-energy sum and separation energy are roughly equivalent.removal energy. On factor that tends to stabilize Eq. (1) with respect to input assumptions is that some of the uncertainties are self-compensating. If, for example, the neutron multiplicity and/or energy input to the filter is too high, the separation-energy decreases, and vice versa.

Another factor that must be kept in mind is that many of the assumptions that are involved in the filter protocol are averages, and therefore do not adequately account for fluctuations in the distributions. Because of the exponential decrease in yield with increasing E*/A, fluctuations skew the distribution toward lower excitation energies. This effect is

demonstrated in Fig. 12. The upper frame shows the average yield as a function of E*/A bin size (heavy solid line). Superimposed on each bin is a Gaussian approximation to the fluctuation widths that increases with excitation energy (light lines). The effect on the E*/A distribution is shown in the middle frame of Fig. 12, showing the yield (yellow) for the data (solid points) and that for the deconvoluted distribution (red). Over the range up to E*/A ~ 8 MeV there is relative agreement between the two distributions. Above this energy, the most probable E*/A value increasingly falls below that of the average.

Summary

From examination of the existing analyses, it is estimated that as a thermodynamic variable, all of the results are self-consistent over about a 20% range in E*/A. Given this uncertainty, however, there is a remarkable agreement among all of the data sets. In the range E*/A ~ 4-5 MeV, a dramatic change occurs in multifragmentation observables that signals a distinct change in reaction mechanism. Within a phase-transition scenario, this would represent the transition energy. The consistency of the measurements is perhaps best illustrated by the caloric curve analysis of Natowitz in Fig. 13, in which all of the caloric curve measurements, shown in the upper left-hand frame, are decomposed as a function of source mass in the right-hand column. When this decomposition is performed a systematic behavior is revealed that lends greater credence to caloric-curve behavior and can be employed to estimate the compressibility constant K for nuclear matter.

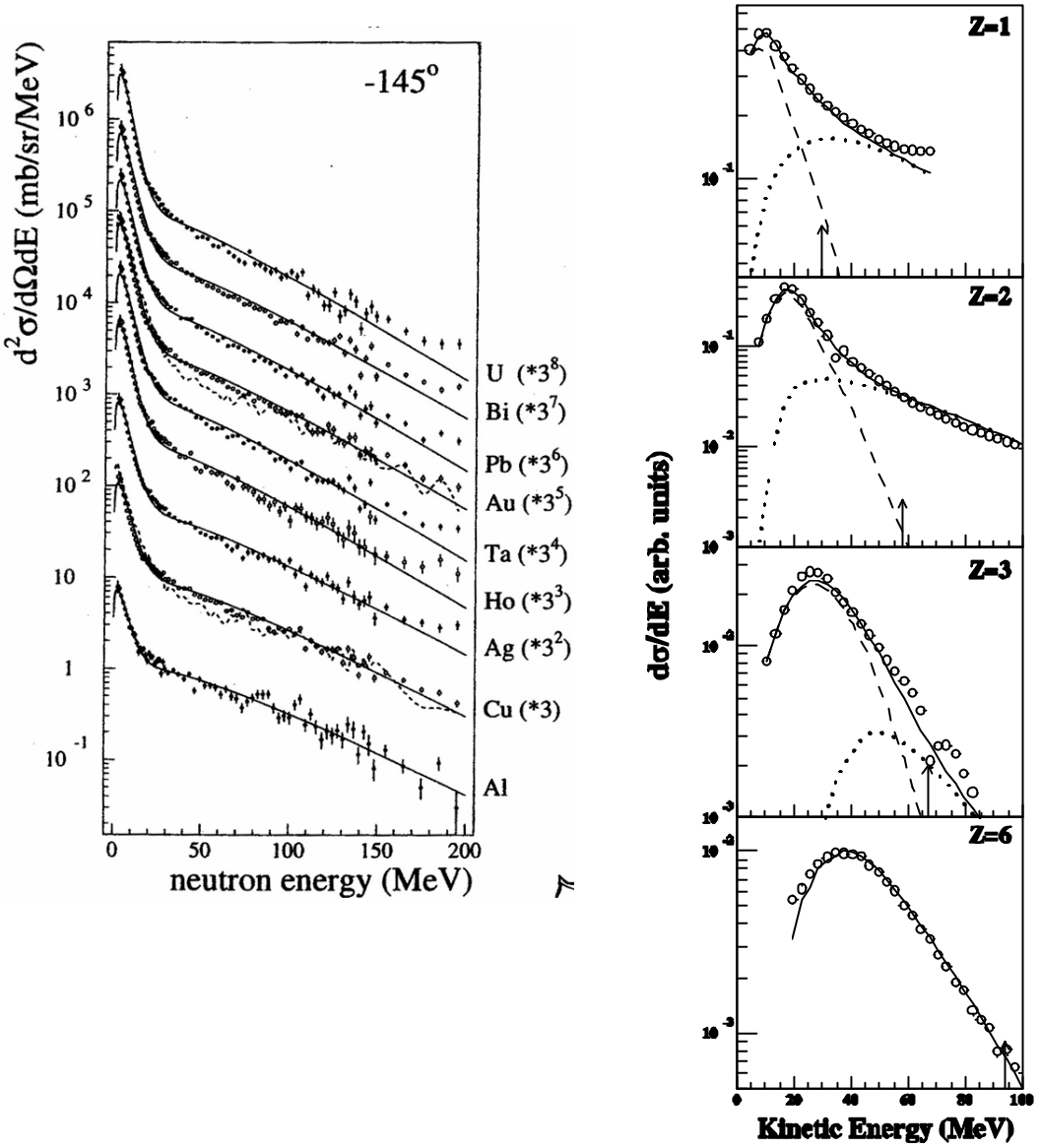
-145°
d²σ/dΩdE (mb/sr/MeV)
neutron energy (MeV)
U (*3⁸)
Bi (*3⁷)
Pb (*3⁶)
Au (*3⁵)
Ta (*3⁴)
Ho (*3³)
Ag (*3²)
Cu (*3)
Al
Z=1
Z=2
Z=3
Z=6
dσ/dE (arb. units)
Kinetic Energy (MeV)

Figure 1.

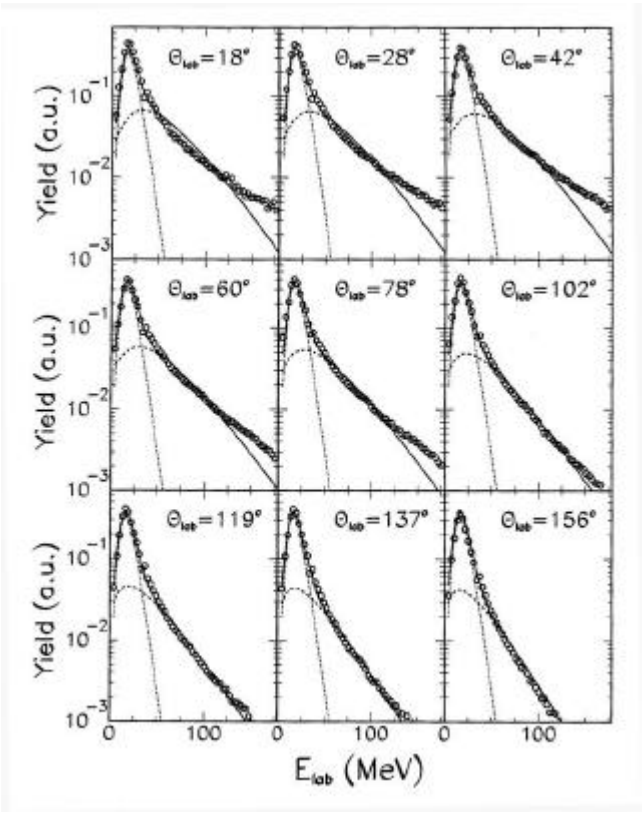
Yield (a.u.)
Θ_{lab}=18°
Θ_{lab}=28°
Θ_{lab}=42°
Θ_{lab}=60°
Θ_{lab}=78°
Θ_{lab}=102°
Θ_{lab}=119°
Θ_{lab}=137°
Θ_{lab}=156°
E_{lab} (MeV)

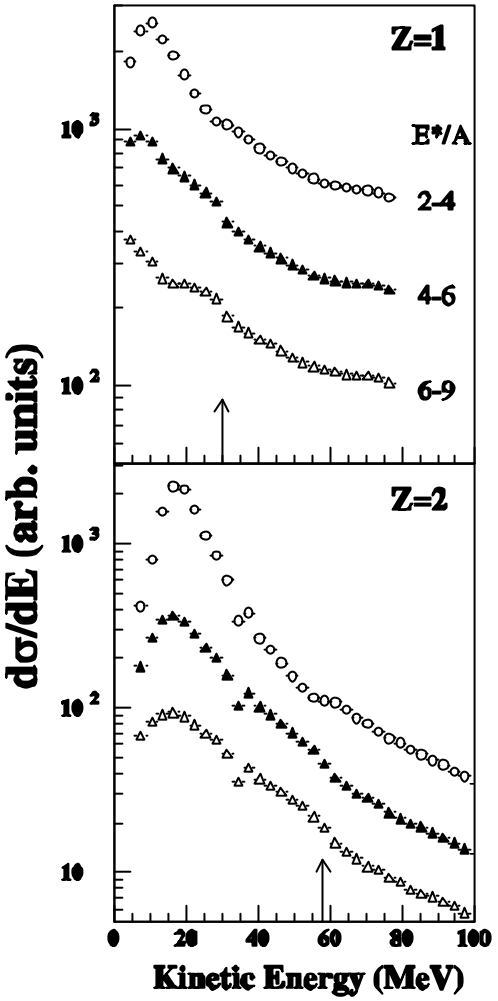
Z=1
E*/A
2-4
4-6
6-9
Z=2
dσ/dE (arb. units)
Kinetic Energy (MeV)

Figure 2

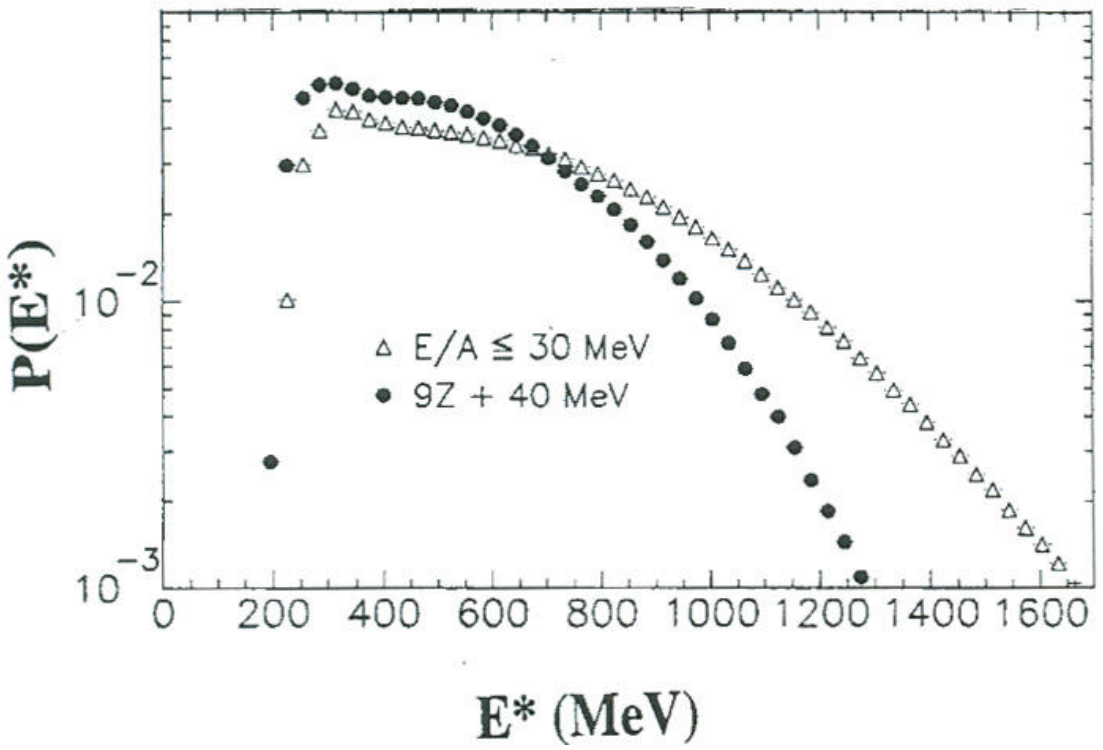
P(E*)
10^-2
10^-3
△ E/A ≦ 30 MeV
● 9Z + 40 MeV
0
200
400
600
800
1000
1200
1400
1600
E* (MeV)

Figure 3

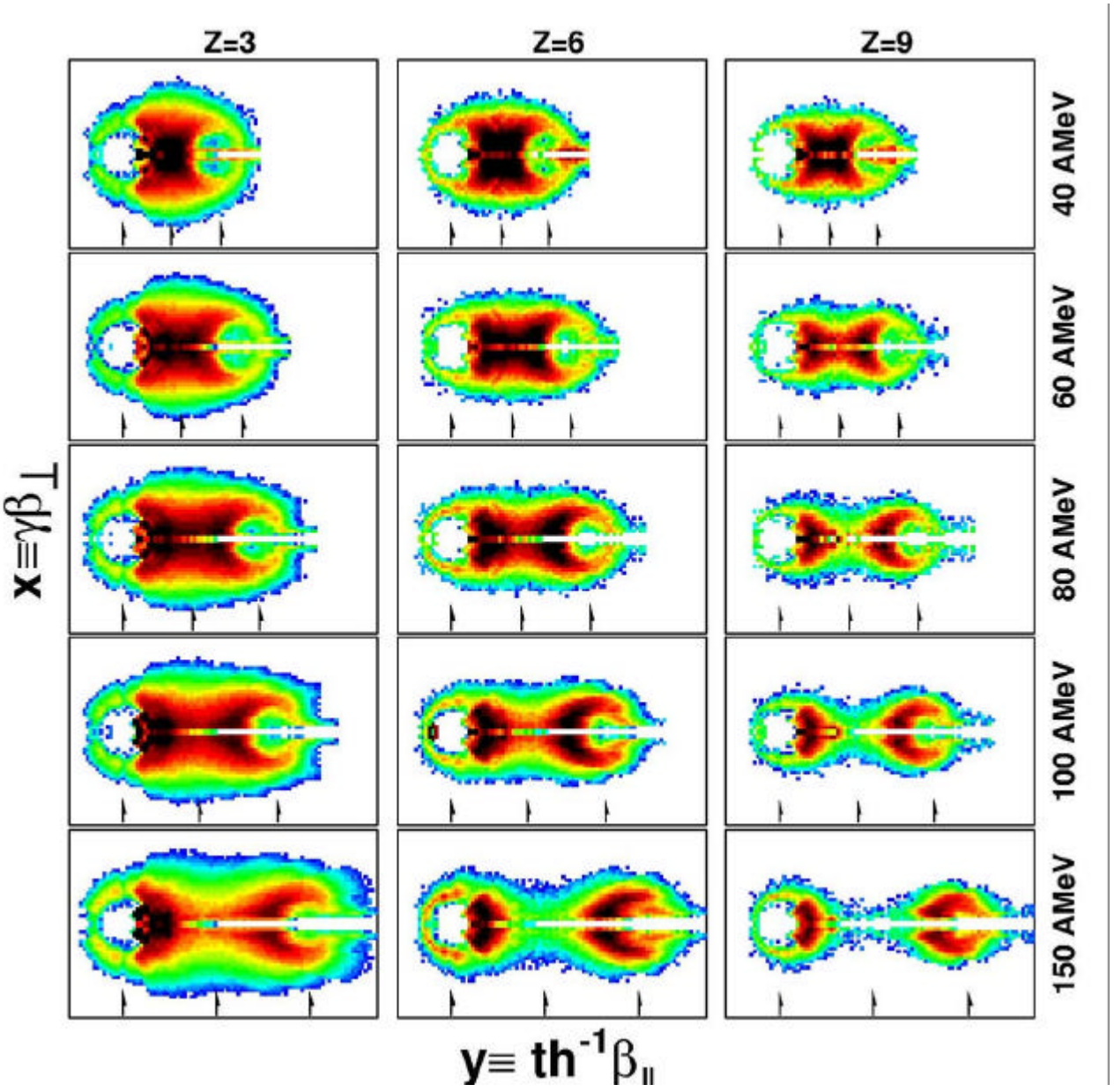

Figure 4

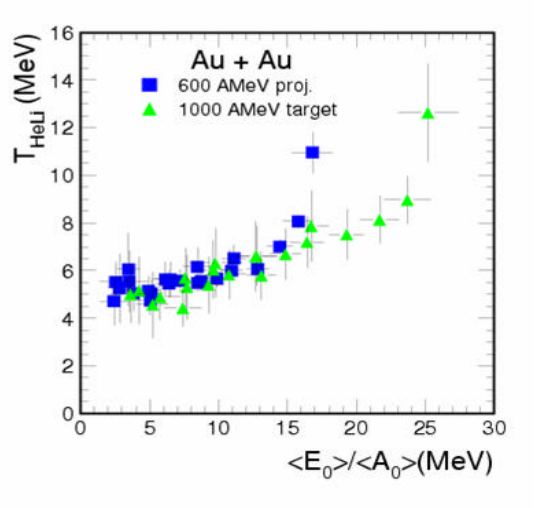
Au + Au
600 AMeV proj.
1000 AMeV target
T_HeLi (MeV)
<E0>/<A0>(MeV)

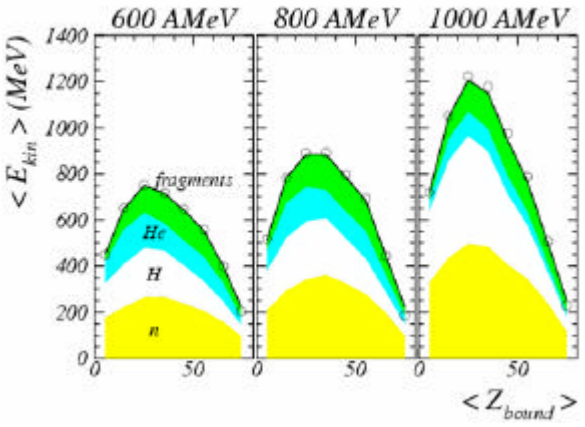
600 AMeV
800 AMeV
1000 AMeV
< E_kin > (MeV)
fragments
He
H
n
< Z_bound >

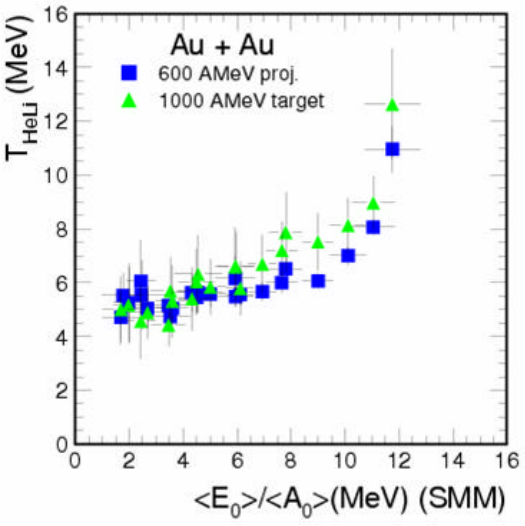
Au + Au
600 AMeV proj.
1000 AMeV target
T_HeLi (MeV)
<E0>/<A0>(MeV) (SMM)

Fig. 5

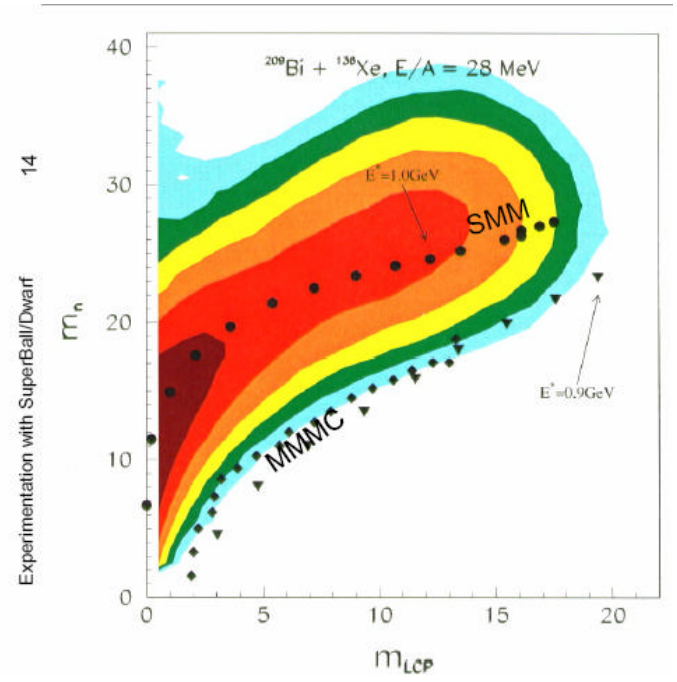
Experimentation with SuperBall/Dwarf
14
^{209}Bi + ^{136}Xe, E/A = 28 MeV
E*=1.0GeV
SMM
E*=0.9GeV
MMMC
m_n
m_{LCP}
0
10
20
30
40
0
5
10
15
20

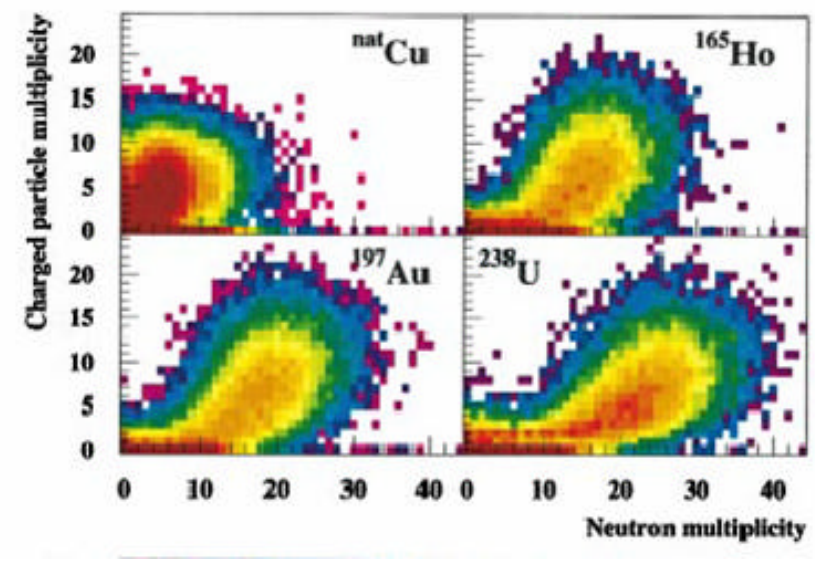
Charged particle multiplicity
Neutron multiplicity
^{nat}Cu
^{165}Ho
^{197}Au
^{238}U
0
5
10
15
20
0
10
20
30
40

Figure 6

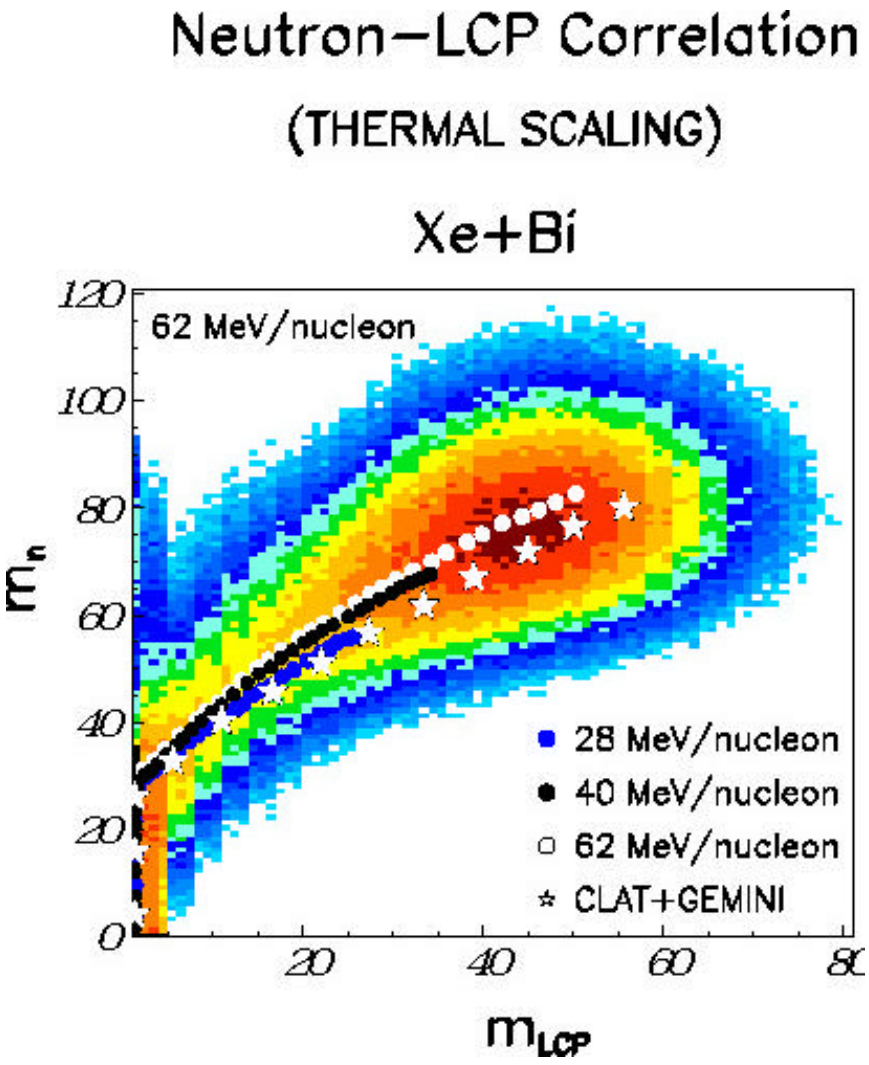
Neutron–LCP Correlation
(THERMAL SCALING)
Xe+Bi
62 MeV/nucleon
28 MeV/nucleon
40 MeV/nucleon
62 MeV/nucleon
CLAT+GEMINI
m_n
m_{LCP}
0
20
40
60
80
100
120

Figure 7

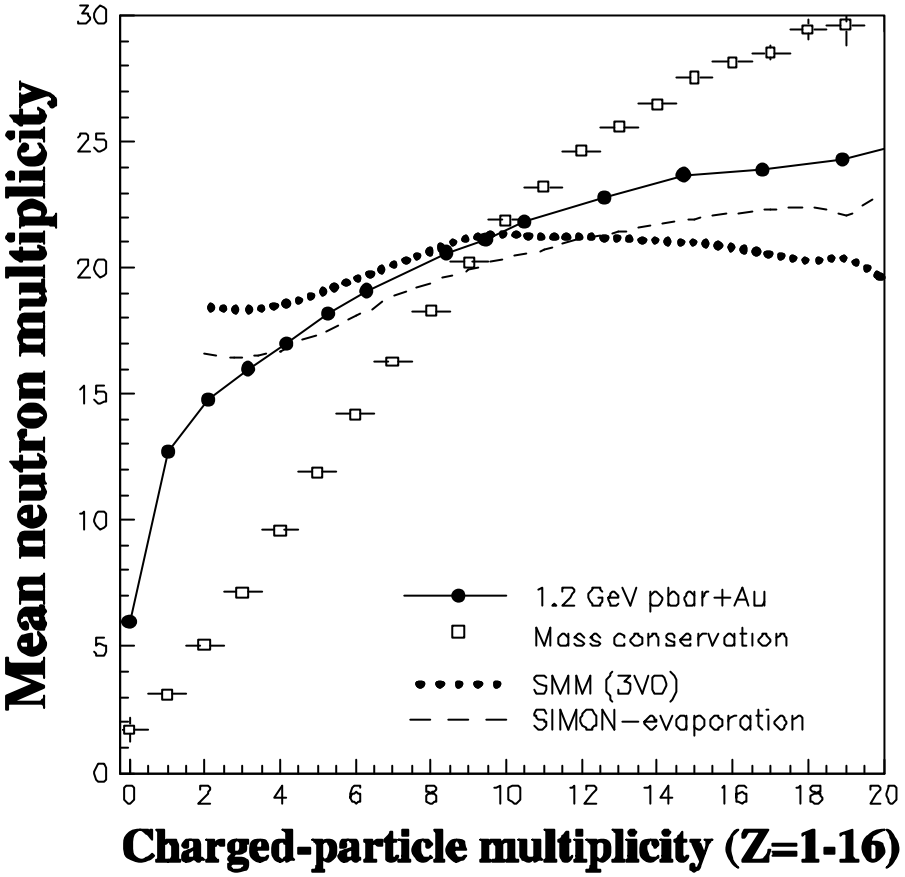
Mean neutron multiplicity
Charged-particle multiplicity (Z=1-16)
1.2 GeV pbar+Au
Mass conservation
SMM (3V0)
SIMON−evaporation
0
5
10
15
20
25
30
0
2
4
6
8
10
12
14
16
18
20

Figure 8

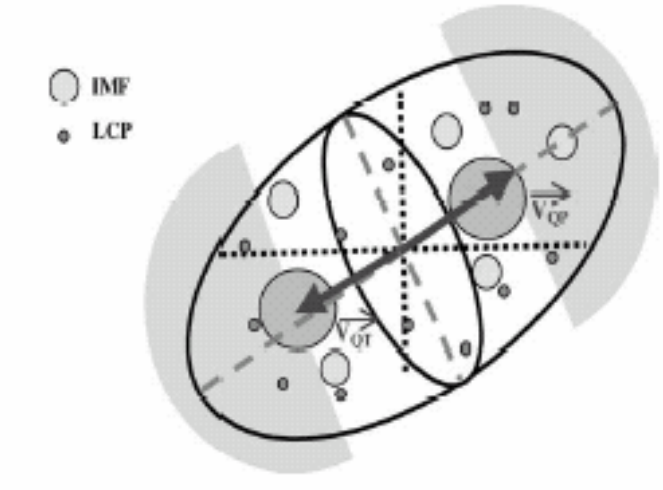
IMF
LCP
V_{QP}
V_{QT}

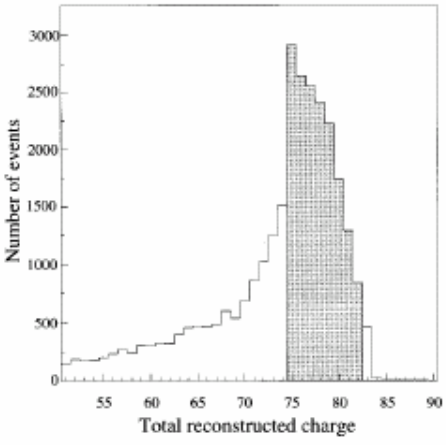
Number of events
Total reconstructed charge

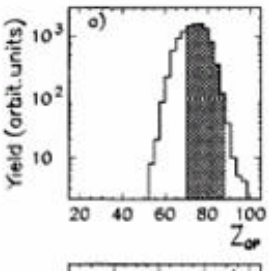
Yield (orbit. units)
Z_{QP}

Figure 9

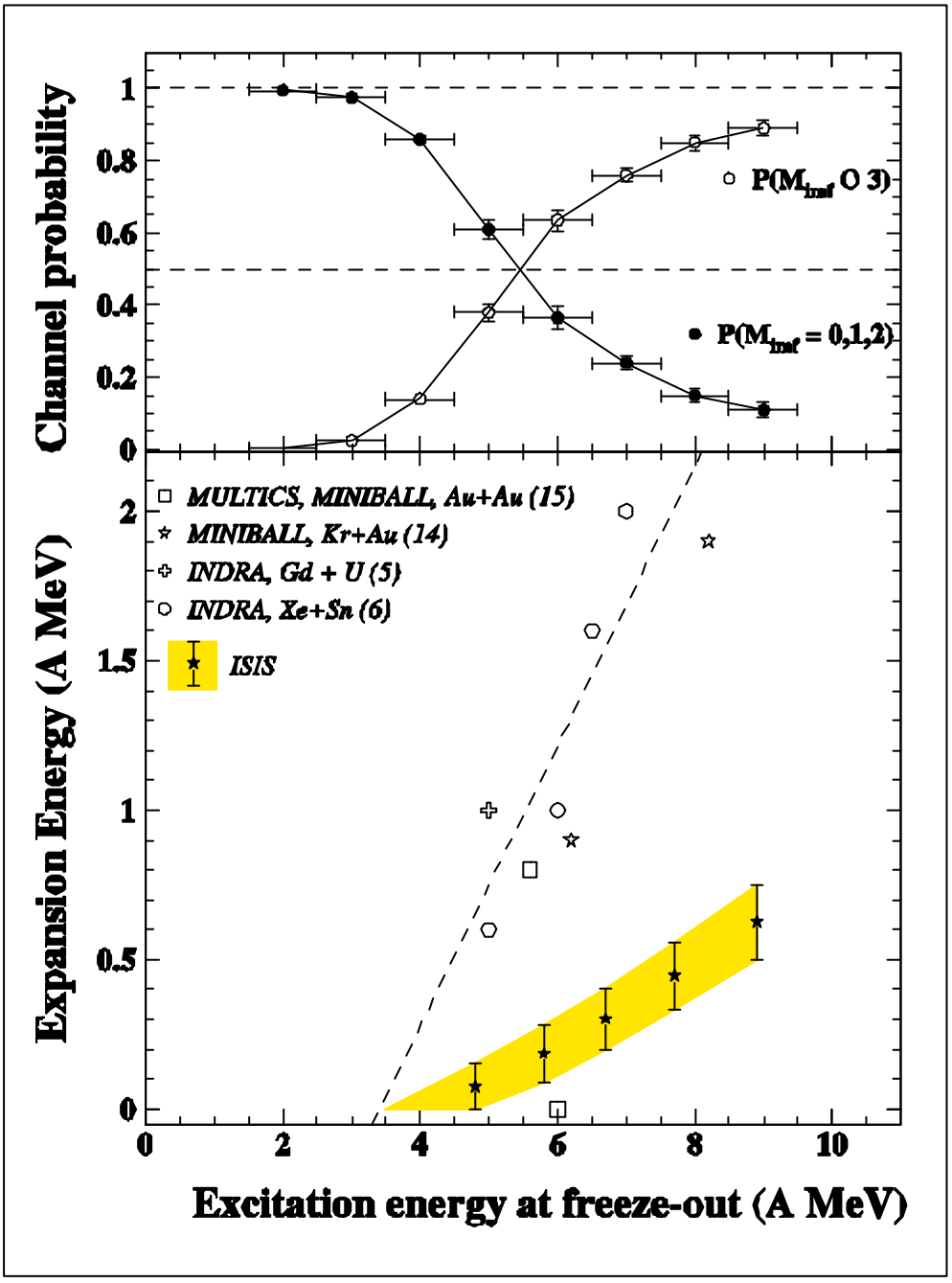
Channel probability
P(M_inf O 3)
P(M_inf = 0,1,2)
Expansion Energy (A MeV)
MULTICS, MINIBALL, Au+Au (15)
MINIBALL, Kr+Au (14)
INDRA, Gd + U (5)
INDRA, Xe+Sn (6)
ISIS
Excitation energy at freeze-out (A MeV)

Figure 10

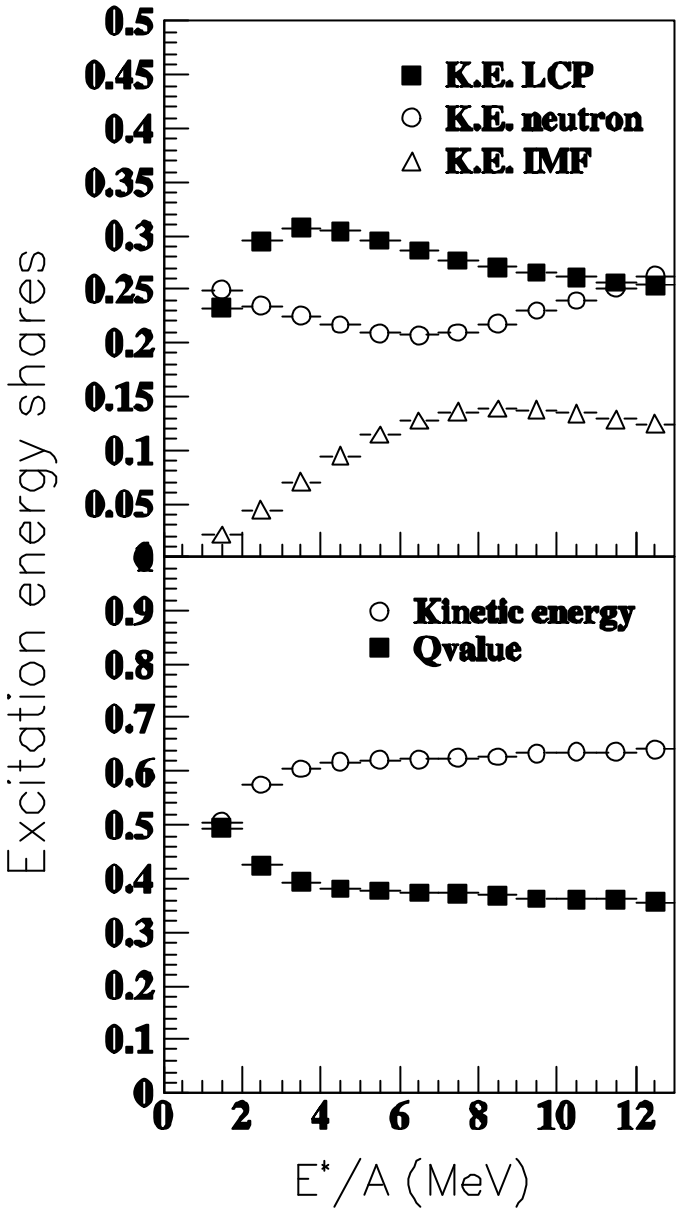
Excitation energy shares
K.E. LCP
K.E. neutron
K.E. IMF
Kinetic energy
Qvalue
E*/A (MeV)

Figure 11

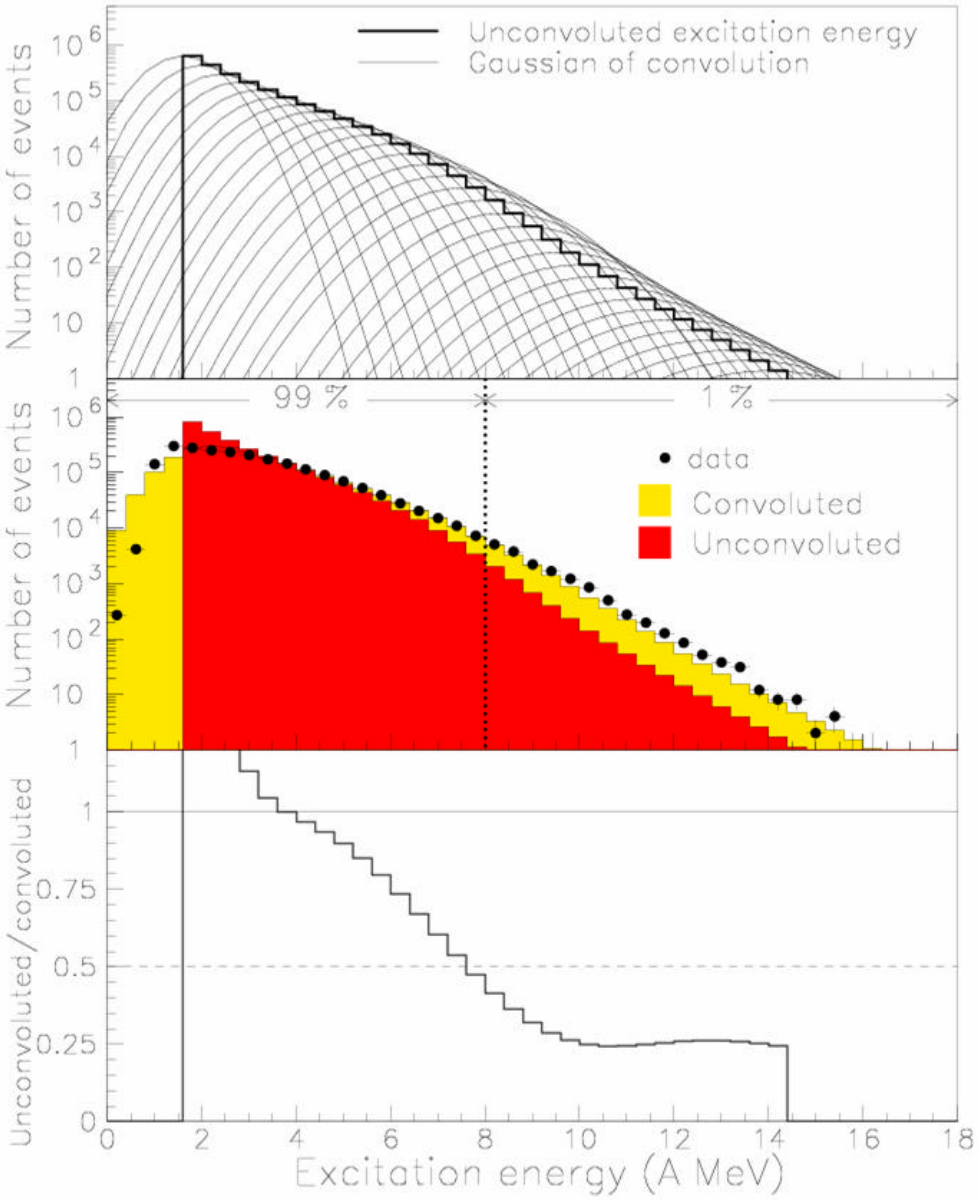
Unconvoluted excitation energy
Gaussian of convolution
Number of events
99 %
1 %
data
Convoluted
Unconvoluted
Number of events
Unconvoluted/convoluted
Excitation energy (A MeV)

Figure 12

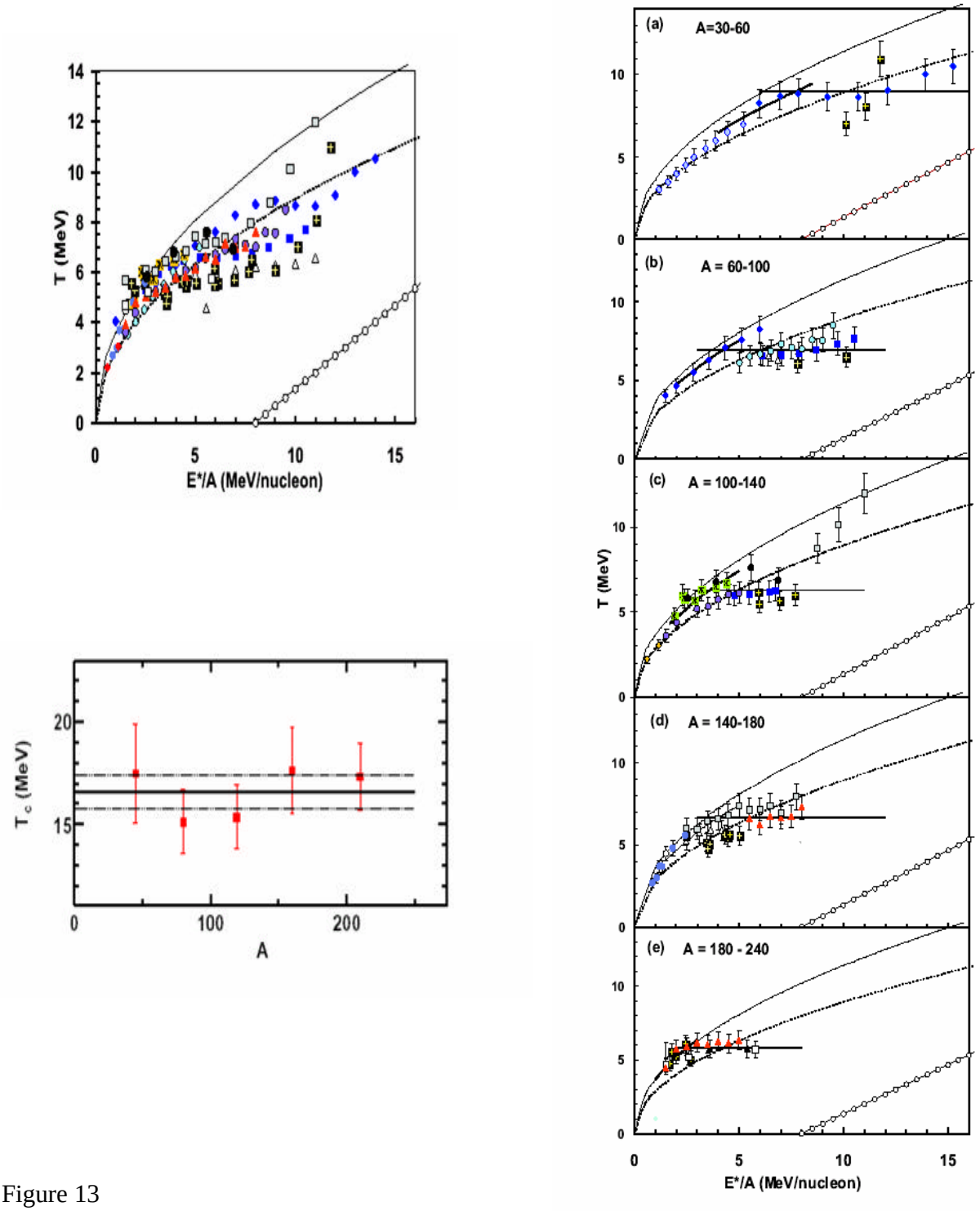
T (MeV)
E*/A (MeV/nucleon)
(a) A=30-60
(b) A = 60-100
(c) A = 100-140
(d) A = 140-180
(e) A = 180 - 240
T (MeV)
E*/A (MeV/nucleon)
T_c (MeV)
A

Figure 13